Astronomy & Astrophysics manuscript no. 6032
October 6, 2006

Tests of stellar model atmospheres by optical interferometry IV

VINCI interferometry and UVES spectroscopy of Menkar ⋆

M. Wittkowski[1], J. P. Aufdenberg[2], T. Driebe[3], V. Roccatagliata[4], T. Szeifert[5], and B. Wolff[1]

[1] European Southern Observatory, Karl-Schwarzschild-Strasse 2, D-85748 Garching bei München, Germany, e-mail: mwittkow@eso.org
[2] National Optical Astronomy Observatory, 950 North Cherry Avenue, Tucson, AZ 85719, USA
[3] Max-Planck-Institut für Radioastronomie, Auf dem Hügel 69, 53121 Bonn, Germany
[4] Max-Planck-Institut für Astronomie, Königsstuhl 17, 69117 Heidelberg, Germany
[5] European Southern Observatory, Casilla 19001, Santiago 19, Chile

Received . . . ; accepted . . .

ABSTRACT

Aims. We present coordinated near-infrared K-band interferometric and optical spectroscopic observations of the M 1.5 giant α Cet (Menkar) obtained with the instruments VINCI and UVES at the Paranal Observatory. Spherically symmetric PHOENIX stellar model atmospheres are constrained by comparison to our interferometric and spectroscopic data, and high-precision fundamental parameters of Menkar are obtained.

Methods. Our high-precision VLTI/VINCI observations in the first and second lobes of the visibility function directly probe the model-predicted strength of the limb darkening effect in the K-band and the stellar angular diameter. The high spectral resolution of UVES of R = 80 000 − 110 000 allows us to confront in detail observed and model-predicted profiles of atomic lines and molecular bands.

Results. We show that our derived PHOENIX model atmosphere for Menkar is consistent with both the measured strength of the limb-darkening in the near-infrared K-band and the profiles of spectral bands around selected atomic lines and TiO bandheads from 370 nm to 1000 nm. At the detailed level of our high spectral resolution, however, noticeable discrepancies between observed and synthetic spectra exist. We obtain a high-precision Rosseland angular diameter of $\Theta_{\rm Ross}$=12.20 mas ± 0.04 mas. Together with the Hipparcos parallax of 14.82 mas ± 0.83 mas, it corresponds to a Rosseland radius of $R_{\rm Ross}$=89 ± 5 $R_\odot$, and together with the bolometric flux based on available spectrophotometry, to an effective temperature of $T_{\rm eff}$=3795 K ± 70 K. The luminosity based on these values is L=1460 $L_\odot$ ± 300 $L_\odot$. Relying on stellar evolutionary tracks, these values correspond to a mass M = 2.3 $M_\odot$ ± 0.2 $M_\odot$ and a surface gravity $\log g$=0.9 ± 0.1 (cgs).

Conclusions. Our approach illustrates the power of combining interferometry and high-resolution spectroscopy to constrain and calibrate stellar model atmospheres. The simultaneous agreement of the model atmosphere with our interferometric and spectroscopic data increases confidence in the reliability of the modelling of this star, while discrepancies at the detailed level of the high resolution spectra can be used to further improve the underlying model.

Key words. Techniques: interferometric – Stars: late-type – – Stars: atmospheres – Stars: fundamental parameters – Stars: individual: α Cet

1. Introduction

Stellar atmosphere models predict in general the spectrum emerging from every point of a stellar disc. These models are often based on assumptions of a stationary 1-dimensional plane-parallel atmospheric structure (e.g., ATLAS 9 models, Kurucz 1993), or a stationary spherically symmetric structure (e.g., PHOENIX models, Hauschildt & Baron 1999; Hauschildt et al. 1999).

Confrontation of model atmospheres with observations is often performed by spatial integration of the model radiation field over the whole stellar disc, spectral integration to broadband colours and/or spectrograms of different spectral resolution, and subsequent comparison to observed broadband photometry, spectro-photometry, or (high-resolution) spectroscopy. For instance, Tripicchio et al. (1997, 1999) measured the D resonance lines of neutral sodium and the KI resonance line at 7699 Å to test MARCS (Gustafsson et al. 1975; Plez et al. 1992, 1993) model atmospheres that include photospheric and chromospheric effects. Valenti et al. (1998) performed a least-squares fit of synthetic spectra to echelle spectroscopy of an M 3.5 dwarf. They successfully constrained the model atmosphere by using the 7087 Å TiO bandhead and five atomic Fe I and Ti I lines between 8674 Å and 8692 Å. Decin et al. (2003) compared infrared spectroscopy obtained with ISO-SWS with MARCS stellar model atmosphere predictions to estimate fundamental stellar parameters.

⋆ Based on observations collected at the European Southern Observatory, Chile, under program number 71.D-0370(A,B).

Optical interferometry provides a further and more direct test of stellar atmosphere models by resolving the stellar disc and measuring the centre-to-limb intensity variation (CLV) across the stellar disc. Interferometric measurements of stellar CLVs include, for instance, those by Hanbury Brown et al. (1974), Haniff et al. (1995), Quirrenbach et al. (1996), Burns et al. (1997), Hajian et al. (1998), Wittkowski et al. (2001, 2004, 2006), Perrin et al. (2004a, 2004b), Woodruff et al. (2004), Fedele et al. (2005), and Aufdenberg et al. (2005). The combination of interferometry and high-resolution spectroscopy to constrain stellar model atmospheres, as suggested and presented, for instance, by Aufdenberg et al. (2003) and van Belle et al. (2003), has so far been surprisingly rare, although this approach can provide a very strong test of theoretical models.

Here, we present coordinated near-infrared *K*-band interferometry obtained with the VLTI instrument VINCI and high-resolution (R up to 110 000) optical spectroscopy obtained with the VLT echelle spectrograph UVES of the M 1.5 giant α Cet (Menkar, HD 18884, HR 911, HIP 14135). We demonstrate the advantage of combined interferometry and high-resolution spectroscopy to test and constrain `PHOENIX` model atmospheres (Hauschildt & Baron 1999; Hauschildt et al. 1999). We derive a set of high-precision fundamental parameters of α Cet.

α Cet is a red giant with spectral type M 1.5 III (Morgan & Keenan 1973), a parallax of π=14.82 mas ± 0.83 mas, a V magnitude of 2.54 (both from Perryman & ESA 1997), and a small variability of ΔV=0.09 (Kholopov et al. 1999). Decin et al. (2003) derived an effective temperature of $T_{\rm eff}$=3740 ± 140 K, a surface gravity of $\log g$=0.95 ± 0.25, a mass of $M/M_{\odot}$=2.69 ± 1.61, a [Fe/H]= 0.00 ± 0.30, a luminosity of L=1455 ± 328 $L_{\odot}$, and a (limb-darkened) angular diameter Θ of 12.52 ± 0.79 mas, based on a comparison of ISO SWS data to `MARCS` models. Alonso et al. (2000) derived a (limb-darkened) angular diameter of 12.59 ± 0.36 mas and an effective temperature of 3704 ± 39 K by means of the infrared flux method (IRFM). Earlier interferometric diameter measurements include those by Dyck et al. (1998: $\Theta_{\rm UD}$ at *K*-band 11.6 ± 0.4 mas; bolometric flux 1.05±0.16 10^{-12} W cm^{-2}), Quirrenbach et al. (1993: $\Theta_{\rm UD}$ at 712 nm, TiO band, 11.95 ±0.23 mas; $\Theta_{\rm UD}$ at 754 nm, continuum, 11.66 ± 0.22 mas), Mozurkewich et al. (1991, 2003: $\Theta_{\rm UD}$ at 800 nm 12.269±0.237 mas; $\Theta_{\rm UD}$ at 550 nm 11.473±0.251 mas; $\Theta_{\rm UD}$ at 451 nm 11.325±0.410 mas).

2. VINCI observations and data reduction

We obtained near-infrared *K*-band interferometric measurements of α Cet in the first and second lobe of the visibility function using the ESO Very Large Telescope Interferometer (VLTI) equipped with the VINCI instrument and the two VLTI siderostats. For a recent technical description of the VLTI, see for instance Glindemann et al. (2003); for the VINCI instrument, see Kervella et al. (2003, 2004).

Between 2 October 2003 and 5 December 2003, 38 visibility measurements were secured in the first lobe of the visibility function using the baseline E0-G0 with an unprojected baseline length of 16 m. Further observations obtained during the same period (11 additional nights during October to December) and using the same 16 m baseline were not used because a consistent interferometric transfer function could not be established with sufficient precision, partly owing to an insufficient time coverage of calibration stars. On 11 & 12 January 2004, four visibility measurements were recorded in the second lobe of the visibility function employing the D0-H0 baseline with an unprojected length of 64 m. Since all our observations cover only a small range of projected baseline angles on the sky (see Table 2), they are not sensitive to possible asymmetries of the stellar disc. Data of α Cet and of several interferometric calibration stars were obtained as series of 500 interferograms with scan lengths of 250 μm and a fringe frequency of 295 Hz. Calibration star details, including the adopted angular diameters, are listed in Table 1.

Table 1. Properties of the used interferometric calibration stars. The references are (D) calibration by Dyck et al. (1996), (B) Bordé et al. (2002), and (K) Kervella et al. (2003).

Calibrator	$\Theta_{\rm UD}$	Ref.	Sp. Type	$T_{\rm eff}$
17 Mon	2.59±0.26	D	K4III	4090
18 Mon	1.86±0.02	B	K0IIIa	4656
19 Ari	2.37±0.03	B	M0III	3690
28 Mon	3.14±0.30	D	K4III	4090
29 Ori	1.92±0.19	D	G8III	4670
30 Gem	2.02±0.03	B	K1III	4581
31 Leo	3.22±0.05	B	K4III	4202
31 Ori	3.56±0.06	B	K5III	4046
6 Leo	2.10±0.03	B	K2.5IIIb	4318
β Cet	5.18±0.06	B	K0III	4656
χ Phe	2.69±0.03	B	K5III	4046
HR 1663	2.69±0.27	D	K5III	3920
η Cet	3.35±0.04	B	K1.5III	4380
η Eri	2.64±0.20	D	K1III	4510
γ^1 Cae	2.31±0.23	D	K3III	4230
α Car	6.45±0.60	D	F0II	7200
HR 1799	2.04±0.20	D	K5III	3920
HR 2311	2.43±0.04	B	K5III	4046
HR 4546	2.53±0.04	B	K3III	4256
HR 6862	2.59±0.05	B	K4.5III	4097
HR 7092	2.81±0.03	B	M0III	3690
ι Cet	3.27±0.04	B	K1.5III	4508
ι Eri	2.12±0.02	B	K0III	4581
ι Hya	3.41±0.05	B	K2.5III	4318
ν^2 CMa	2.38±0.03	B	K1III	4497
α CMa	5.93±0.02	K	A1V	9230
θ CMa	4.04±0.40	D	K4III	4099
ζ Hya	3.33±0.30	D	G9II-III	4559

Mean coherence factors were obtained for each series of interferograms using the VINCI data reduction software, version 3.0, as described by Kervella et al. (2004), employing the results based on the wavelet transforms. Calibrated squared visibility values for α Cet were obtained from the mean coherence factors as described in Wittkowski et al. (2004). A time kernel of 3 hours was used to convolve the measured interferometric transfer function during each night. The computed errors of the squared visibility amplitude take into account the scatter of the single scan's coherence factors, the errors of the diameters

Table 2. Details of our VINCI observations of α Cet (date and time of observation, spatial frequency, azimuth angle of the projected baseline (E of N)), together with the measured squared visibility amplitudes and their errors. The last column denotes the number of successfully processed interferograms for each series.

Date & Time (UT)	Sp. freq [1/″]	az [deg]	V^2	σ_{V^2}	#
2003-10					
-03 4:04:48	22.79	67.9	8.550e-01	1.090e-02	488
-03 4:12:01	23.57	68.6	8.322e-01	1.073e-02	473
-03 4:44:19	26.86	70.7	7.782e-01	1.002e-02	486
-03 4:51:27	27.53	71.1	7.629e-01	9.888e-03	467
-03 5:25:02	30.37	72.4	7.150e-01	9.299e-03	490
-03 5:32:18	30.91	72.5	7.052e-01	9.208e-03	482
-20 6:23:10	35.47	72.8	6.202e-01	2.874e-02	445
-20 6:30:14	35.48	72.7	6.321e-01	2.951e-02	414
-21 5:58:25	35.27	73.1	6.128e-01	1.737e-02	455
-21 6:05:40	35.37	73.0	6.062e-01	1.718e-02	471
-22 3:29:06	26.81	70.7	7.951e-01	1.044e-02	442
-22 3:36:30	27.51	71.1	7.712e-01	9.284e-03	425
-22 4:15:05	30.73	72.5	7.169e-01	1.117e-02	408
-22 4:22:10	31.24	72.7	7.073e-01	1.302e-02	354
-24 5:34:53	35.04	73.2	6.278e-01	2.122e-02	479
-24 5:48:19	35.30	73.1	6.222e-01	2.146e-02	351
-29 5:47:00	35.47	72.9	6.420e-01	1.237e-02	348
-29 5:58:10	35.47	72.7	6.573e-01	8.384e-03	467
2003-11					
-27 3:14:20	34.87	73.3	6.435e-01	6.270e-03	492
-27 3:21:37	35.05	73.2	6.393e-01	6.255e-03	488
2003-12					
-04 1:37:03	31.51	72.7	7.067e-01	7.754e-03	488
-04 1:44:08	31.98	72.9	7.033e-01	7.740e-03	479
-04 2:17:53	33.82	73.2	6.689e-01	7.695e-03	482
-04 2:24:54	34.12	73.3	6.560e-01	7.413e-03	476
-04 3:03:23	35.24	73.1	6.384e-01	7.146e-03	483
-04 3:10:23	35.34	73.1	6.367e-01	7.200e-03	475
-04 4:19:06	34.78	71.5	6.393e-01	7.430e-03	437
-04 4:26:25	34.56	71.3	6.437e-01	9.154e-03	388
-05 0:05:53	23.74	68.7	8.474e-01	1.024e-02	338
-05 0:13:52	24.59	69.3	8.037e-01	2.597e-02	93
-05 1:35:55	31.70	72.8	7.091e-01	7.531e-03	471
-05 1:43:08	32.16	72.9	6.969e-01	7.743e-03	467
-05 2:28:03	34.39	73.3	6.520e-01	7.566e-03	447
-05 2:35:39	34.65	73.3	6.548e-01	9.280e-03	358
-05 3:23:51	35.48	72.8	6.304e-01	7.116e-03	469
-05 3:49:52	35.32	72.3	6.388e-01	7.630e-03	424
-06 3:48:38	35.29	72.2	6.360e-01	8.405e-03	482
-06 3:55:49	35.16	72.0	6.376e-01	8.533e-03	483
2004-01					
-12 1:00:54	141.86	72.7	1.281e-02	6.655e-04	275
-12 1:13:28	141.57	72.4	1.300e-02	6.133e-04	299
-13 1:28:57	140.38	71.9	1.324e-02	6.934e-04	275
-13 1:40:23	139.25	71.6	1.365e-02	6.689e-04	270

of the calibration stars, and the variation of the interferometric transfer function over the night. Observational details and the calibrated squared visibility values with their errors are listed in Table 2. The inverse of the mean wavenumber of the α Cet observations was 2.187 μm.

As a first characterisation of the angular diameter of α Cet, we calculated best-fitting angular diameters $\Theta_{\rm UD}$ and $\Theta_{\rm FDD}$ for models of a uniform disc (UD: $I = 1$ for $0 < \mu < 1$; else 0) and a fully darkened disc (FDD: $I = \mu$). Here, $\mu = \cos\theta$ is the cosine of the angle between the line of sight and the normal of the surface element of the star. The angular diameter ($\Theta_{\rm UD}$ or $\Theta_{\rm FDD}$) is the only free parameter. Synthetic squared visibility amplitudes were calculated using the broadband VINCI sensitivity function (cf. the description in Wittkowski et al. 2004, 2006). We obtained $\Theta_{\rm UD}$=11.95 mas ± 0.06 mas with a reduced χ^2_ν(UD) value of 3.35, and $\Theta_{\rm FDD}$=13.32 mas ± 0.12 mas with χ^2_ν(FDD)=10.20.

Furthermore, we used an empirical parametrisation of the limb-darkened stellar intensity profile as $I(\mu) = \mu^\alpha$ (cf. Hestroffer et al. 1997), and simultaneously determined the best-fitting values for the limb-darkened angular diameter $\Theta_{\rm LD}$ and the limb-darkening parameter α. We obtain $\Theta_{\rm LD}$=12.27 mas ± 0.05 mas and α=0.24 ±0.03 with χ^2_ν(LD)=1.01. This parametrisation of a limb-darkened intensity profile closely resembles the CLVs (centre-to-limb variations) that are obtained by stellar model atmospheres based on plane-parallel geometry, where the atmosphere is optically thick for any viewing angle, and the intensity steeply drops to zero at the stellar limb. In this case, the Rosseland angular diameter and our obtained limb-darkened angular diameter, which corresponds to the 0% intensity level, can be considered equivalent (cf. the discussion in Wittkowski et al. 2004).

These results already show that our interferometric data cannot be well described by uniform or fully darkened disc models, but are well consistent with a limb-darkened intensity profile that has a strength of the limb-darkening (α=0.24) that is closer to that of a uniform disc (α=0) than a fully-darkened disc (α=1) model. Figure 1 shows our measured visibility points together with the described UD, FDD, and LD models, as well as with the predictions by `PHOENIX` and `ATLAS` 9 model atmospheres (derived and described below).

3. UVES observations and data reduction

We obtained high-resolution spectroscopy of α Cet with the echelle spectrograph UVES mounted on the UT2 (KUEYEN) telescope of the ESO VLT in service mode on 11 August 2003. We used the dichroic settings 346+580 nm and 437+860 nm with slit widths of 0.4″ (blue arm) and 0.3″ (red arm). This corresponds to a spectral resolution of 80 000 in the blue and 110 000 in the red, respectively. The details of our UVES data with numbers of individual integrations for each central wavelength of the UVES grating and exposure times are listed in Table 3.

For all the observations, the bias and inter-order background were subtracted. The spectral orders were extracted, flat-fielded, and wavelength calibrated with recipes available from the ESO UVES pipeline. The "average extraction method" of the pipeline has been used, which uses a uniform average of the pixel values across the slit. Statistical errors have been calculated from the variance obtained with this extraction

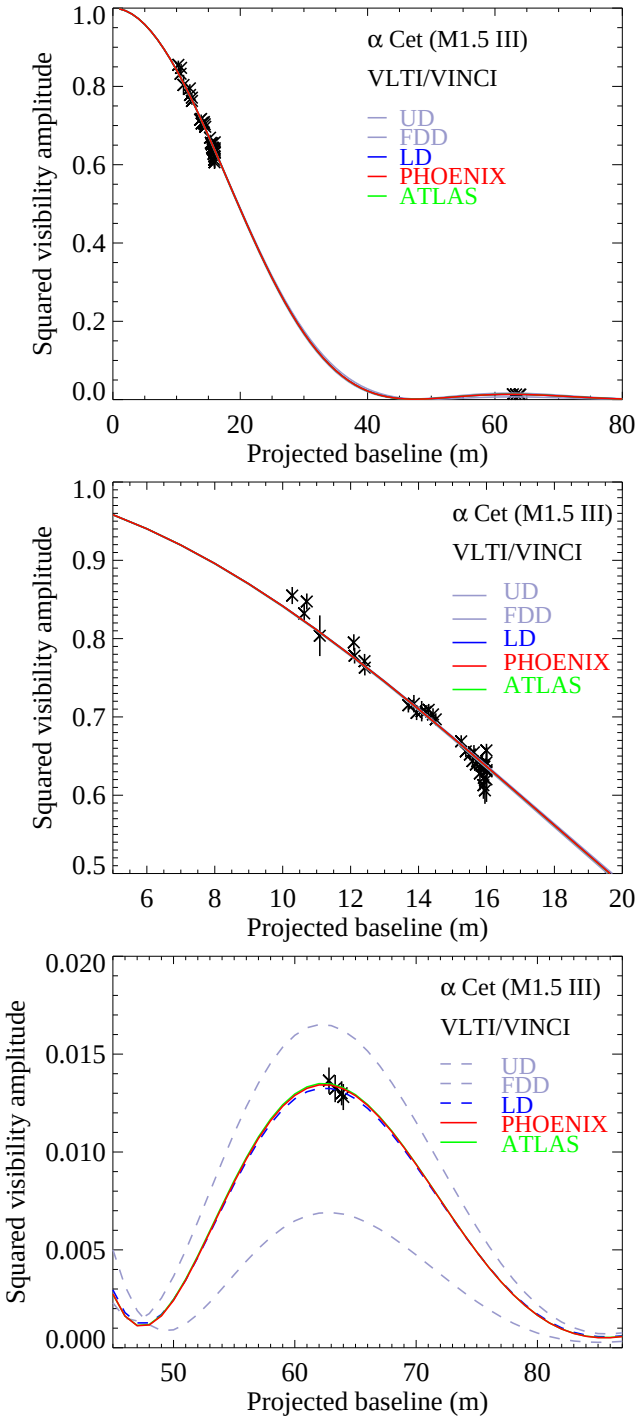

Fig. 1. Squared visibility amplitudes and error bars of α Cet obtained with VLTI/VINCI, together with best-fitting models of a uniform disc (upper dashed light blue line), a fully darkened disc (lower dashed light blue line), a parametrisation $I = \mu^{\alpha}$ with α=0.24 (dashed blue line) and of PHOENIX and ATLAS 9 model atmosphere predictions (solid red and green lines). The PHOENIX model shown has parameters $T_{\rm eff}$=3800 K, log g=1.0, $M = 2.3 M_{\odot}$; the ATLAS 9 model $T_{\rm eff}$=3800 K, log g=1.0 (see text for more details). The upper panel shows the full range of the visibility function, while the middle panel is an enlargement of the obtained squared visibility values in the first lobe, and the bottom panel shows an enlargement of the low squared visibility function in the 2nd lobe. Our measurements are sig-

Table 3. Overview of our UVES observations of α Cet obtained on 11 August 2003 between 9:30h and 9:40h UT. Shown are the central wavelength $\lambda_{\rm central}$ of each of the UVES gratings and the recorded wavelength ranges $\lambda_{\rm min} - \lambda_{\rm max}$. The spectra of the red arm of UVES were recorded using two different detectors, and are thus split into the two wavelength ranges. Also given are, for each grating, the spectral resolution $R = \lambda/\Delta\lambda$, the number of individual exposures and their exposure times, as well as the maximum signal-to-noise ratio $S/N_{\rm max}$ reached.

$\lambda_{\rm central}$ (nm)	$\lambda_{\rm min} - \lambda_{\rm max}$ (nm)	R	# of exp.	Exp. time of each exp. (s)	$S/N_{\rm max}$
346	305-387	80 000	2	120.0	500
437	374-499	80 000	2	3.7	280
580	477-577/ 583-683	110 000	7	1.5	800
860	665-853/ 867-1040	110 000	2	0.5	280

method. The extracted spectra have been flux-calibrated using averaged response curves as provided by the Quality Control Group of ESO Garching. This calibration provides a relative flux calibration with an accuracy of ~10-20% within each spectrum. Absolute flux values for our UVES spectrum of α Cet have not been obtained. Finally, multiple exposures of each setting have been averaged. The resulting signal-to-noise ratios S/N vary across the spectra, and the maximum S/N values reached for each grating are listed in Table 3. The correction to heliocentric velocity has been determined by the pipeline analysis to $v_{\rm helio}$=-28.7 km/sec, so that the relation between arriving wavelength from the star λ_0 and observed wavelength $\lambda_{\rm obs}$ is $\lambda_{\rm obs} = \lambda_0(1 + v_{\rm helio}/c)$.

4. Atmosphere models for α Cet

We use new, fully line-blanketed spherical, hydrostatic atmosphere models with solar photospheric abundances (Grevesse & Noels 1993) obtained with version 13 of the PHOENIX code (Hauschildt & Baron 1999; Hauschildt et al. 1999). Feast et al. (1990) discussed that solar metallicity is appropriate for giants in the solar neighbourhood and found that the (rms) scatter of the metallicity of local giants is less than 0.08. This is consistent with the [Fe/H]= 0.00 ± 0.30 derived by Decin et al. (2003) for α Cet. The microturbulence for all our new models is 2 km s^{-1}. The three most important input parameters for our spherical model are the effective temperature, the surface gravity, and the stellar mass. For each model used, we tabulate the flux integrated over the stellar disc from 300 nm to 1050 nm in steps of 0.001 nm (for comparison to our high spectral resolution UVES data). Furthermore, we tabulate monochromatic intensity profiles at 64 viewing angles for wavelengths from 1.8 μm to 2.5 μm in steps of 0.5 nm (for comparison to our VINCI interferometric data).

For comparison, we use intensity profiles predicted by standard plane-parallel hydrostatic ATLAS 9 model atmospheres from the Kurucz CD-ROMs (Kurucz 1993), as in Wittkowski et al. (2001, 2004, 2006), as well. The Kurucz CD-ROMs include

tabulated monochromatic intensity profiles for 17 angles in 1221 frequency intervals ranging from 9.09 nm to 160 000 nm. In the range of the VINCI near-infrared K-band filter, the frequencies are sampled in steps corresponding to 10 nm. These data values are available as grids of effective temperature and surface gravity (the mass is not an input parameter for a plane-parallel model), and for different chemical abundances and microturbulent velocities. For comparison, we use the grid with solar chemical abundances and a microturbulence of 2 km s^{-1}.

For a further description of the use of the PHOENIX and ATLAS models for comparison to interferometric data obtained with VINCI, for the calculation of synthetic visibility values, and for effects of plane-parallel and spherical geometries on the obtained angular diameter, we refer to Wittkowski et al. (2004, 2006).

4.1. The bolometric flux of α Cet

We have constructed a composite spectral energy distribution for α Cet by combining absolute spectrophotometry in the optical (Glushneva et al. 1998a, 1998b) and infrared (Cohen et al. 1996) to estimate the bolometric energy flux, $f_{\rm bol}$, at the Earth (see Fig. 2). Note that an absolute flux calibration of our UVES echelle spectrum has not been obtained (see Sect. 3), so that we rely on spectrophotometry from other sources to derive the bolometric flux of α Cet. We directly integrate the tabulated irradiance from 322.5 nm to 1037.5 nm (5 nm resolution) and 1.26 μm to 35 μm (0.02 μm to 0.18 μm resolution), using a five-point Newton-Cotes integration formula. Between 1.04 μm and 1.26 μm, the irradiance at 20 nm intervals is estimated by linearly interpolating, in $\log\lambda - \log F_\lambda$ space, between the end points of the two data sets. We assume all the irradiance data are uncertain at the level of 5%. This procedure results in $f_{\rm bol}$=$(1.01 \pm 0.05)\,10^{-12}$ W cm^{-2}. At a distance of 67 pc, the interstellar foreground extinction in the direction of α Cet is likely to be quite low. HD 18883 (B7 V), at a distance of 134 pc, has a measured colour excess, $E(B-V)$=0.03, from space-based UV photometry (Savage et al. 1985) and is 0.3° from α Cet. Therefore, adopting $E(B-V)$=0.015 and an average R_V=3.1 Galactic reddening curve (Cardelli et al. 1989) as a best estimate for the extinction towards α Cet, the bolometric flux becomes $f_{\rm bol}$=$(1.03 \pm 0.07)\,10^{-12}$ W cm^{-2}, including the uncertainty in the extinction. This value is well consistent with the estimate by Dyck et al. (1998) of $(1.05\pm0.16)\,10^{-12}$ W cm^{-2} based on broadband photometry alone.

4.2. Comparison of PHOENIX model predictions to available spectrophotometry

We have compared synthetic spectral energy distributions (SEDs) from PHOENIX models with the absolute spectrophotometry used to derive the bolometric flux above. The goodness of the SED fit is largely insensitive to specific values of the surface gravity and mass in the model grid. The least-squares fits for the grid and application of the F-test provide the following mean values and 1 σ uncertainties: $T_{\rm eff}$=3800 ± 100 K for $\Theta_{\rm Ross}$=12.0 ± 0.7 mas. These uncertainties are correlated, so that low $T_{\rm eff}$ values correspond to high $\Theta_{\rm Ross}$ values and vice versa. Figure 2 shows the spectrophotometric data compared to the synthetic SED based on the model with mean parameters mentioned above. Differences between observed and synthetic SED are largest at optical ($\lambda < 0.7$ nm) wavelengths. With the Hipparcos parallax, the angular diameter of $\Theta_{\rm Ross}$=12.0 ± 0.7 mas corresponds to a Rosseland linear radius of $R_{\rm Ross}$=$87 \pm 10\,R_\odot$ and luminosity $\log(L)$=$3.16 \pm 0.18\,L_\odot$. Relying on the evolutionary tracks from Girardi et al. (2000), the position of the star in the theoretical HR diagram results in a mass $M/M_\odot$=2.3 ± 0.5 (see Fig. 1 in Wittkowski et al. 2004). From the mass and the Rosseland radius, we derive a surface gravity of $\log g$=0.9 ± 0.2.

4.3. Comparison of model predictions to our VINCI data

We derive best-fitting limb-darkened (0% intensity) diameters $\Theta_{\rm LD}$ to our VINCI data for different PHOENIX model atmospheres with parameters $T_{\rm eff}$, $\log g$, and M that lie within ranges consistent with the estimates above. The procedure used is the same as described in Wittkowski et al. (2004, 2006). Table 4 lists the considered model parameters and the resulting best-fitting $\Theta_{\rm LD}$, $\Theta_{\rm Ross}$, and reduced χ^2_ν values for each model. The ratio between the outermost model layer corresponding to $\Theta_{\rm LD}$ and the $\tau_{\rm Ross}$=1 layer corresponding to $\Theta_{\rm Ross}$ is read from the PHOENIX model atmospheric structure as described in Wittkowski et al. (2004). The precision of the best-fitting diameter values for a given model atmosphere listed in Table 4 is relatively high (0.4%). We have shown by a study of night-to-night variations that such high-precision diameter values based on VINCI data are generally reliable (Wittkowski et al. 2006). Also, the different considered PHOENIX models with variations of $T_{\rm eff}$, $\log g$, and M result in consistent Rosseland angular diameters, so that no uncertainty due to the choice of model parameters needs to be added.

For comparison, we derive the best-fitting limb-darkened diameter based on the corresponding plane-parallel ATLAS 9 model as well. For plane-parallel geometry, $\Theta_{\rm LD}$ and $\Theta_{\rm Ross}$ can be considered equivalent (Wittkowski et al. 2004). However, the definition of the Rosseland diameter is more precise for models based on spherical geometry (cf. Wittkowski et al. 2006). Here, the resulting Rosseland angular diameters based on the PHOENIX and ATLAS 9 models agree very well.

The corresponding synthetic K-band visibility curve and thus the resulting χ^2_ν values are not sensitive to variations of $T_{\rm eff}$, $\log g$, and M within the considered ranges. The good χ^2_ν values of 0.99 shows that the measured and model-predicted strength of the limb-darkening effect in the K-band agree well. Figure 1 shows the measured squared visibility amplitudes together with the PHOENIX and ATLAS model prediction. Also shown are the simple models of a uniform disc, fully darkened disc, and the parametrisation $I = \mu^\alpha$ as discussed in Sect. 2.

The high-precision Rosseland angular diameter obtained from the comparison of the PHOENIX model atmospheres to our VINCI data of $\Theta_{\rm Ross}$=12.20 ± 0.04 mas corresponds with the Hipparcos parallax to a linear Rosseland radius of

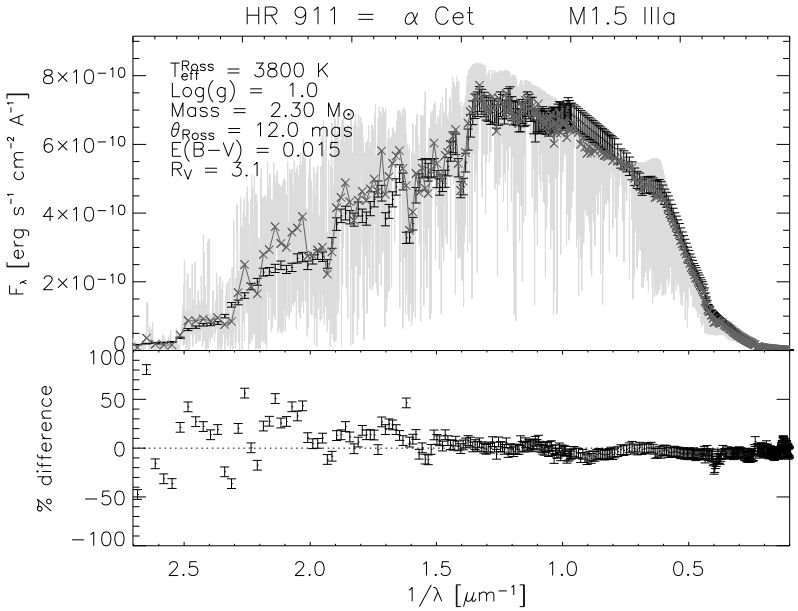

Fig. 2. (Top) The observed spectral energy distribution of α Cet (shown as error bars) from Glushneva et al. (1998a, 1998b) and Cohen et al. (1996) compared with synthetic spectrophotometry ('x' symbols) derived from the PHOENIX model (shown in grey at high-resolution) with the mean parameters listed in the text. (Bottom) The percentage difference between the observed and synthetic spectrophotometry in each wavelength bin.

Table 4. Best fitting angular diameters of α Cet based on a comparison of our VINCI data to different model atmospheres.

Model parameters			Θ_{LD}	Θ_{Ross}	χ^2_ν
T_{eff} [K]	$\log g$	$M/M_\odot$	[mas]	[mas]	
PHOENIX models:					
3800	1.0	2.3	12.60 ± 0.04	12.20 ± 0.04	0.99
3700	1.0	2.3	12.60 ± 0.04	12.20 ± 0.04	0.98
3900	1.0	2.3	12.60 ± 0.04	12.20 ± 0.04	0.99
3800	0.5	2.3	12.95 ± 0.04	12.19 ± 0.04	0.99
3800	1.5	2.3	12.43 ± 0.04	12.21 ± 0.04	0.99
3800	1.0	2.0	12.63 ± 0.04	12.20 ± 0.04	0.99
3800	1.0	2.6	12.58 ± 0.04	12.20 ± 0.04	0.99
ATLAS 9 model for comparison:					
3750	1.0	/	12.20 ± 0.04	12.20 ± 0.04	0.99

R_{Ross}=89 ± 5 $R_\odot$. Here, the error is by far dominated by the error of the bolometric flux. Our VINCI value for Θ_{Ross} together with the bolometric flux derived above results in an effective temperature of T_{eff}=3795 ± 70 K. R_{Ross} and T_{eff} result in a luminosity $\log L/L_\odot$=3.16 ± 0.08 (L=1460 $L_\odot$ ± 300 $L_\odot$). These values are well consistent but more precise than the values estimated above by a comparison of the PHOENIX models with available spectrophotometry. Based on the stellar evolutionary tracks by Girardi et al. (2000), we can estimate a mass of $M/M_\odot$=2.3 ± 0.2 and a surface gravity of $\log g$=0.9 ± 0.1 (cgs).

4.4. Comparison of model predictions to our UVES spectra

We consider in the following the spherical PHOENIX model atmosphere as described above with parameters T_{eff}=3800 K, $\log g$=1.0, and $M = 2.3 M_\odot$ because it is closest to the model parameters derived by comparison to our VINCI data and well describes the measured strength of the limb-darkening in the K-band. Here, we compare the model-predicted spectrum in several bandpasses to our measured UVES spectrum to investigate to what extent the same model that is consistent with our interferometric data is consistent with our high-resolution spectroscopic data as well.

We use four dominant TiO bandheads around 5598Å, 7054Å, 7088Å, and 7126Åfor our analysis. In addition, we have selected 6 bands around dominant atomic lines of Fe I (3683Å, 5447Å, 6945Å), Ca I (4227Å), and Ti I (5966Å, 9675Å) that cover all gratings used for our UVES spectrum and span a total range from 360 nm to 1000 nm. Profiles of atomic lines and TiO bandheads such as these are good indicators of stellar model atmosphere parameters, most importantly, effective temperature and surface gravity (e.g., Valenti et al. 1998).

Calibration of spectral resolution and wavelength The wavelength scales of the synthetic spectra were corrected for the air refraction index, for the Earth's motion and rotation, and for the radial velocity of α Cet of v_{rad}=-26.08 km/sec (Famaey et al. 2005). For each bandpass separately, the synthetic PHOENIX spectrum was broadened by convolution with a rotational pro-

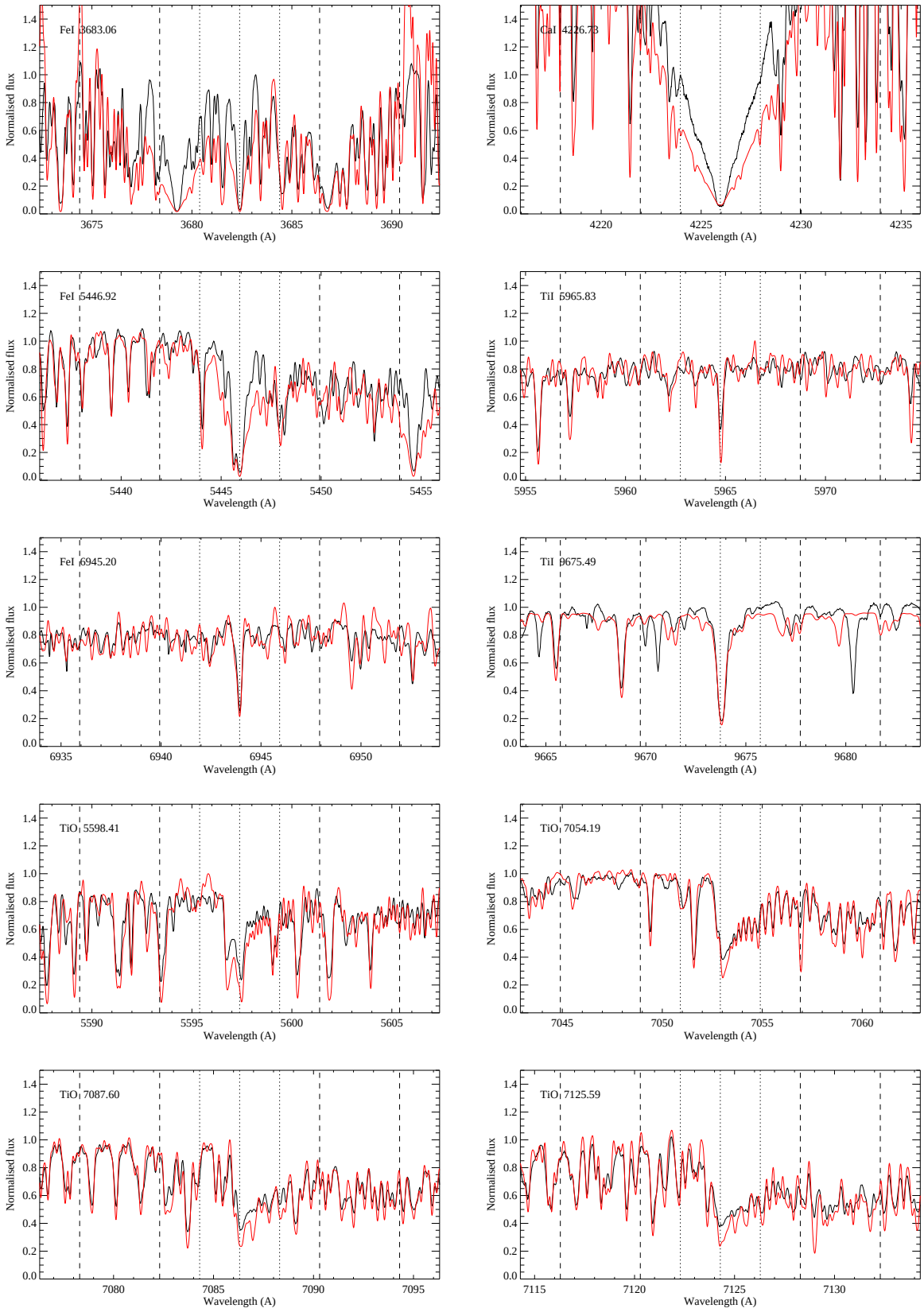

Fig. 3. Observed UVES spectrum (black) together with the synthetic spectrum (red) for each bandpass considered. The parameters of the spherical PHOENIX model used are $T_{\rm eff}$=3800 K, log g=1.0, M = 2.3 $M_{\odot}$, and solar chemical abundance. The vertical dotted lines denote the central wavelength and bandpass used to compute the χ^2_{ν} and integral $W_{\rm obs}/W_{\rm model}$ values in Table 5. The vertical dashed lines denote the bandpasses blueward and redward of the central bandpass that are used to adjust the scale factor f between model spectrum and measured spectrum and to normalise the equivalent width.

Table 5. Bandpasses used for the comparison of PHOENIX model predictions to our UVES spectrum. Listed are the central wavelength $\lambda_{\rm air}$, the identification (ID), the obtained wavelength shift $\Delta\lambda$, the scale factor f between observed and model-predicted spectrum, the reduced χ^2_ν value, and the ratio of observed and model-predicted equivalent width. The scale factors f are derived in blue and red bandpasses at $[-8..-4]$ Å and [4..8] Å with respect to the central wavelength. The χ^2_ν values are then derived in bandpasses [−2..2]Å around $\lambda_{\rm air}$. The equivalent widths are the integrals of the central bandpasses after normalisation of the spectrum to unity using the integral of the blue and red bandpasses.

$\lambda_{\rm air}$ Å	ID	$\Delta\lambda$ Å	$f_{\rm norm}$	χ^2_ν	$W_{\rm obs}/W_{\rm model}$
5598.41	TiO	-0.031	0.89	13378	0.70
7054.19	TiO	-0.006	1.09	530	1.01
7087.60	TiO	-0.010	1.04	1071	0.80
7125.59	TiO	-0.029	1.07	674	0.91
3683.06	Fe I	-0.002	1.09	17496	3.4
4226.73	Ca I	-0.004	0.68	169	0.91
5446.92	Fe I	-0.009	0.87	32299	0.47
5965.83	Ti I	-0.037	0.84	7051	0.96
6945.20	Fe I	-0.007	1.20	718	0.69
9675.49	Ti I	-0.073	1.21	188	0.79

file using $v \sin i$=3 km/sec, which is the mean value for M 0 giants (Munari et al. 2001). It was also broadened with a Gaussian profile to match the spectral resolution of the observation given in Table 3. Due to possible residuals of α Cet's radial velocity, and residuals of the synthetic line positions, small offsets between the synthetic and observed wavelength scales can remain. We have used the IDL routine `crscor` from the IUE library (http://archive.stsci.edu/iue) to cross-correlate the observed and synthetic spectra for each bandpass used and to derive remaining wavelength shifts. The resulting wavelength shifts as listed in Table 5 are of the order of 0.01Å (corresponding to 0.6 km/sec at 5000Å) and are small for the purpose of our comparison.

Comparison of observed and synthetic spectra An absolute flux calibration of our UVES spectra was not obtained, leading to an unknown scale factor between observed and synthetic spectrum. We have determined, by a standard least-squares fit, the best scale factor f to match observed and synthetic spectra in two bandpasses blueward and redward of each central bandpass. For a cool giant, we cannot find good continuum bands close to the central wavelengths. The bandpasses used for this adjustment have a standard width of 4Å and standard central wavelengths -6Å and +6Å with respect to the central wavelength, and inevitably contain spectral features as well. The resulting χ^2_ν value between observed and synthetic spectra was calculated for each central bandpass. The normalised factors $f_{\rm norm}$ and the χ^2_ν values are listed in Table 5. The variations of $f_{\rm norm}$ are generally consistent with the relative uncertainty of the flux calibration of our UVES spectrum of 10-20% for each spectrum as quoted in Sect. 3. In addition to the direct χ^2 comparison between observed and synthetic spectra, we calculate the ratio between measured and predicted equivalent width $W_{\rm obs}/W_{\rm model}$ as a measure of the consistency of the integrated line strengths. The equivalent width is derived, separately for synthetic and observed spectra, by integrating the spectrum over the central bandpass after normalisation to unity using the integral of the red and blue bandpasses.

Figure 3 shows the final comparison of observed and synthetic spectra for each considered bandpass. Our PHOENIX model describes the measured spectrum around all selected features well qualitatively. We have inspected a number of additional features across the total wavelength range of our UVES spectrum and find comparable agreement. However, on the detailed level of the high spectral resolution obtained, measurement and model prediction exhibit differences that dominate the resulting χ^2_ν value in Table 5. These differences include different strengths of individual lines, line positions, and features that appear in the observed spectrum, but not in the synthetic spectrum, and vice versa. It is known that synthetic and observed stellar spectra at this detailed level show discrepancies such as these and that relatively large χ^2_ν values are thus to be expected for a direct comparison (see, e.g., Kučinskas et al. 2005). The integrated quantity $W_{\rm obs}/W_{\rm model}$ has a mean value of 0.80 and standard deviation 0.16 (excluding the 3683.06 Å Fe I bandpass where the blending of different spectral features is strongest), i.e., the observed spectral features have, over all, a lower strength than predicted by the model at the level of $1.25\,\sigma$.

A variation of model parameters $\log g$, and M within the uncertainties that remain from the comparison to our VINCI data do not lead to significant changes of Fig. 3 and on the χ^2_ν and $W_{\rm obs}/W_{\rm model}$ values in Table 3. These parameters can thus not be further constrained by the comparison to our UVES spectrum. A variation of $T_{\rm eff}$ (model values 3750 K, 3800 K, 3850 K, 3900 K; other model parameters unchanged) allows us to estimate the effective temperature of α Cet to $T_{\rm eff} \approx 3820 \pm 50$ K both based on the χ^2_ν or the $W_{\rm obs}/W_{\rm model}$ values as a function of $T_{\rm eff}$. This estimate is based on the comparison of observed and synthetic spectral lines/bands and is consistent with the estimate based on the best-fitting diameter derived from the interferometric data and the bolometric flux derived from available spectrophotometry as described above.

There are three major limitations to a stronger constraint of the model parameters. Firstly, an absolute flux calibration of the UVES spectrum was not obtained, and the relative flux calibration within each spectrum reaches a precision of not better than 10-20%. Secondly, for cool giants, the selected spectral features are not isolated and the bandpasses used are inevitably contaminated by several other lines; nearby true continuum bandpasses are not available. Finally, the total differences between observed and synthetic spectrum for our bandpasses, as characterised by the χ^2_ν values in Table 5, are dominated by detailed effects other than the main model parameters $T_{\rm eff}$, $\log g$, and M.

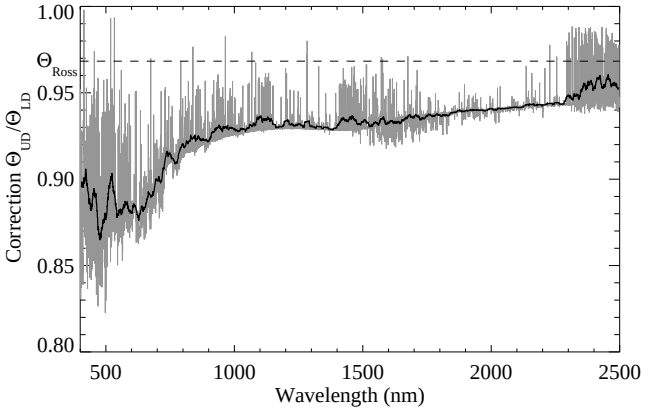

Fig. 4. Correction factors from the 0% LD diameter Θ_{LD} to the UD diameter based on our derived PHOENIX model for α Cet with parameters T_{eff}=3800 K, $\log g$=1, and $M/M_{\odot}$=2.3. The dashed line denotes the Rosseland diameter Θ_{Ross} with respect to the 0% intensity diameter Θ_{LD}, which is 0.968 for this model. The thin grey line shows the full resolution of our PHOENIX model file (5Å), and the solid black line is reduced to a resolution of 20 nm.

Table 6. UD diameters predicted for several previously used bandpasses based on our derived PHOENIX model for α Cet with parameters T_{eff}=3800 K, $\log g$=1, $M/M_{\odot}$=2.3, solar chemical abundance, and Θ_{LD}=12.60 mas. We estimate the accuracy of the model predictions to be ≤ 5%, see text for details on the calculation.

λ_c nm	$\delta\lambda$ nm	Θ_{UD}^{Model} mas	$\Theta_{UD}^{Lit.}$ mas	Reference
2187	400	11.90	11.95 ± 0.06	Direct fit in this work
450	20	11.24	11.33 ± 0.29	Mozurkewich et al. (1991)
451	20	11.24	11.33 ± 0.41	Mozurkewich et al. (2003)
550	20	11.09	11.47 ± 0.25	Mozurkewich et al. (2003)
712	12	11.31	11.95 ± 0.23	Quirrenbach et al. (1993)
754	5	11.52	11.66 ± 0.22	Quirrenbach et al. (1993)
800	20	11.60	12.25 ± 0.16	Mozurkewich et al. (1991)
800	20	11.60	12.27 ± 0.24	Mozurkewich et al. (2003)
2200	400	11.90	11.6 ± 0.4	Dyck et al. (1998)

4.5. Comparison of model prediction to previous diameter measurements

Several UD diameter measurements of α Cet based on long-baseline interferometry have previously been obtained (see Sect. 1). Here, we use our derived PHOENIX model of α Cet (T_{eff}=3800 K, $\log g$=1, $M/M_{\odot}$=2.3, solar chemical abundance, Θ_{LD}=12.60 mas) to predict the UD diameter at the previously used bandpasses. The correction factor from the 0% (LD) diameter to the UD diameter is calculated so that both visibility curves, the UD curve and the curve based on the model atmosphere, match where $|V|^2 = 0.3$, as previously done by, e.g., Hanbury Brown et al. (1974), Quirrenbach et al. (1996), and Wittkowski et al. (2001). The choice to match the visibility curves at $|V|^2 = 0.3$ is arbitrary, and the accuracy of the resulting correction factor may decrease if most measured visibility data were obtained at other parts of the visibility curve. We average the correction factors over rectangular bandpasses with central wavelength λ_c and width $\delta\lambda$. The exact shape of the bandpasses used for the previous observations and the exact signal processing of the different instruments is not taken into account. We estimate the total error resulting from these simplifications to be less than about 5%. Figure 4 shows the resulting correction factors for the wavelength range from 400 nm to 2500 nm. Table 6 lists the previously obtained interferometric UD diameter measurements of α Cet compared to the prediction by our derived PHOENIX model for each specific bandpass used. Only the measurements at 550 nm and 800 nm by Mozurkewich et al. (1991, 2003) and the measurement at 712 nm (TiO band) by Quirrenbach et al. (1993) are not consistent within 1 σ with the nominal value of our model prediction, but still within the estimated ∼ 5% uncertainty of our prediction. The discrepancy at the TiO bandpass may either be caused by an imperfect match of the exact instrumental bandpass and signal processing (as here the strength of the limb-darkening effect changes rapidly), or by an imperfect model description of the spatial structure of the layers where TiO molecules reside. It has been reported that the use of different line list combinations of molecules lead to significantly different model structures and spectra, in particular in the optical where TiO bands are important (Allard et al. 2000; Kučinskas et al. 2005).

Table 7. Fundamental parameters of the M 1.5 giant α Cet based on the analysis in this paper. The mass and surface gravity rely on the evolutionary tracks by Girardi et al. (2000).

Parameter	Value
Rosseland angular diameter	Θ_{Ross} = 12.20 ± 0.04 mas
Rosseland linear radius	R_{Ross} = 89 ± 5 $R_{\odot}$
Bolometric flux	f_{bol} = (1.03 ± 0.07) × 10^{-12} W/m^2
Effective temperature	T_{eff} = 3795 ± 70 K
Luminosity	$\log L/L_{\odot}$ = 3.16 ± 0.08
Mass	M = 2.3 ± 0.2 $M_{\odot}$
Surface gravity	$\log g$ = 0.9 ± 0.1 (cgs)

5. Summary and discussion

We have shown that our derived PHOENIX model atmosphere for α Cet (Menkar) with model parameters T_{eff}=3800 K, $\log g$=1, and $M/M_{\odot}$=2.3 is consistent with both the measured strength of the limb-darkening in the broad near-infrared K-band and with the profiles of spectral bands around selected atomic lines and TiO bandheads from 370 nm to 1000 nm. At the detailed level of our high spectral resolution (R up to 110 000), however, noticeable differences of observed and synthetic spectra exist. The discrepancies include differences in the strengths and positions of spectral lines/bands, as well as detailed spectral features that only appear in either the observed or synthetic spectrum. It has previously been reported that the existence of such detailed effects, especially in the optical where TiO bands are important, is known and may be due to, for instance, different line list combinations or treatments of convection (Allard et al. 2000, Kučinskas et al. 2005).

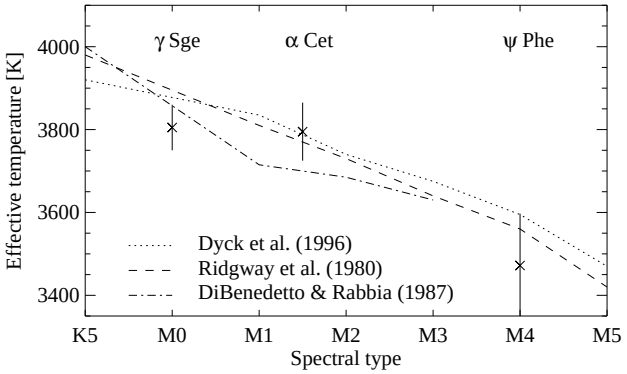

Fig. 5. Measured effective temperature of the M giants γ Sge (Wittkowski et al. 2006), α Cet (present paper), and ψ Phe (Wittkowski et al. 2004) versus spectral type compared to empirical calibrations for giants. The three measurements are consistently obtained by Rosseland diameters based on a comparison of VINCI interferometric data to spherical PHOENIX model atmospheres and bolometric fluxes obtained by careful integration of available spectro-photometry.

The fundamental stellar parameters of α Cet are most constrained by our high-precision angular diameter obtained from the comparison of the PHOENIX atmosphere model with our VINCI data, and the bolometric flux based on available spectrophotometry. This resulting set of fundamental stellar parameters of α Cet is summarised in Table 7. These values are consistent with previous measurements mentioned in Sects. 1 and 4.5, but generally have a higher precision.

Together with the results on the M 4 giant ψ Phe (Wittkowski et al. 2004, Paper II of this series), the M 0 giant γ Sge (Wittkowski et al. 2006, Paper III of this series), and the M 1.5 giant α Cet (present paper), we have consistently obtained sets of high-precision fundamental parameters for these three M giants based on a comparison of VINCI data to spherical PHOENIX model atmospheres. Figure 5 shows the obtained effective temperatures versus spectral types compared to empirical calibrations by Ridgway et al. (1980), Di Benedetto & Rabbia (1987), and Dyck et al. (1996). The measurements are consistent with the empirical calibrations shown at about the $1\,\sigma$ level, but may suggest a flatter temperature slope for early M giants and a stronger decrease of effective temperature for cooler (toward M 4-5) giants.

The studies on these three cool giants also consistently show that the model-predicted strength of the limb-darkening is not significantly affected by the geometry of the model atmosphere for the broad near-infrared *K*-band, and also for narrower visual bandpasses in the case of the NPOI observations of γ Sagittae of Paper III, with the precision of current measurements. Effects from plane-parallel versus spherical geometry thus appear to be more subtle than generally seems to be expected. However, the most precise definition of a meaningful diameter, such as the diameter where the Rosseland-mean optical depth reaches unity, can best be obtained based on a spherical model, as discussed in the articles of this series.

Our results illustrate as well the power of combining interferometry and high-resolution spectroscopy to constrain and calibrate stellar model atmospheres. The newly offered instrument AMBER (Petrov et al. 2003) at the VLTI permits the recording of spectro-interferometric data with a spectral resolution of up to 12 000, i.e., with a resolution that is several orders of magnitudes above that of previous interferometric instruments. This spectral resolution of the newest generation of interferometric instruments, however, is still clearly below that of modern optical spectrographs, such as UVES, or IR spectrographs, such as CRIRES, which provide a spectral resolution of up to $R \geq 100\,000$. It will thus be very valuable to combine AMBER interferometry with UVES or CRIRES highest resolution spectroscopy to constrain stellar models. A limitation of our current study is the lack of an absolute flux calibration of our UVES data, which should be obtained with high precision for such suggested future studies.

Acknowledgements. This work was performed in part (JPA) under contract with the Jet Propulsion Laboratory (JPL) funded by NASA through the Michelson Fellowship Program. JPL is managed for NASA by the California Institute of Technology.

References

Allard, F., Hauschildt, P. H., & Schwenke, D. 2000, ApJ, 540, 1005
Alonso, A., Salaris, M., Arribas, S., Martínez-Roger, C., & Asensio Ramos, A. 2000, A&A, 355, 1060
Aufdenberg, J. P., & Hauschildt, P. H. 2003, Proc. SPIE, 4838, 193
Aufdenberg, J. P., Ludwig, H.-G., & Kervella, P. 2005, ApJ, 633, 424
Bordé, P., Coudé du Foresto, V., Chagnon, G., & Perrin, G. 2002, A&A, 393, 183
Burns, D., Baldwin, J. E., Boysen, R. C., et al. 1997, MNRAS, 290, L11
Cardelli, J. A., Clayton, G. C., & Mathis, J. S. et al. 1989, ApJ, 345, 245
Cohen, M., Witteborn, F. C., Carbon, D. F., et al. 1996, AJ, 112, 2274
Decin, L., Vandenbussche, B., Waelkens, C., et al. 2003, A&A, 400, 709
Di Benedetto, G., & Rabbia, Y. 1987, A&A, 188, 114
Dyck, H. M., Benson, J. A., van Belle, G. T., & Ridgway, S. T. 1996, AJ, 111, 1705
Dyck, H. M., van Belle, G. T., & Thompson, R. R. 1998, AJ, 116, 981
Famaey, B., Jorissen, A., Luri, X., et al. 2005, A&A, 430, 165
Feast, M. W., Whitelock, P. A., & Carter, B. S. 1990, MNRAS, 247, 227
Fedele, D., Wittkowski, M., Paresce, F., et al. 2005, A&A, 431, 1019
Girardi, L., Bressan, A., Bertelli, G., & Chiosi, C. 2000, A&AS, 141, 371
Glindemann, A., Algomedo, J., Amestica, R., et al. 2003, Ap&SS, 286, 35
Glushneva, I. N., Doroshenko, V. T., Fetisova, T. S., et al. 1998, VizieR Online Data Catalog, 3207
Glushneva, I. N., Doroshenko, V. T., Fetisova, T. S., et al. 1998, VizieR Online Data Catalog 3208
Gustafsson, B., Bell, R. A., Eriksson, K., & Nordlund, A. 1975, A&A, 42, 407
Grevesse, N., & Noels, A. 1993, in Origin and Evolution of the Elements, eds. N. Pranto, E. Vangioni-Flam, & M. Casse, Cambridge: Cambridge Univ. Press, 14
Hajian, A. R., Armstrong, J. T., Hummel, C. A., et al. 1998, ApJ, 496, 484

Hanbury Brown, R., Davis, J., Lake, R. J. W., & Thompson, R. J. 1974, MNRAS, 167, 475
Haniff, C. A., Scholz, M., & Tuthill, P. G. 1995, MNRAS, 276, 640
Hauschildt, P. H., & Baron, E., 1999a, J. Comp. Appl. Math 109, 41
Hauschildt, P. H., Allard, F., Ferguson, J., Baron, E., & Alexander, D. R. 1999, ApJ, 525, 871
Hestroffer, D. 1997, A&A, 327, 199
Kervella, P., Gitton, P., Ségransan, D., et al. 2003a, Proc. SPIE, 4838, 858
Kervella, P., Thévenin, F., Morel, P., et al. 2003b, A&A, 408, 681
Kervella, P., Ségransan, D.,& Coudé du Foresto, V. 2004, A&A, 425, 1161
Kholopov, P. N., Samus, N. N., Frolov, M. S., et al. 1999, VizieR Online Data Catalog, 2214
Kurucz, R. 1993, Limbdarkening for 2 km/s grid (No. 13): [+0.0] to [-5.0]. Kurucz CD-ROM No. 17. Cambridge, Mass.: Smithsonian Astrophysical Observatory
Kučinskas, A., Hauschildt, P. H., Ludwig, H. G., et al. 2005, A&A, 442, 281
Morgan, W. W., & Keenan, P. C. 1973, ARA&A, 11, 29
Mozurkewich, D., Johnston, K. J., Simon, R. S., et al. 1991, AJ, 101, 2207
Mozurkewich, D., Armstrong, J. T., Hindsley, R. B., et al. 2003, AJ, 126, 2502
Munari, U., Agnolin, P., & Tomasella, L. 2001, Baltic Astronomy, 10, 613
Perrin, G., Ridgway, S. T., Coudé du Foresto, V., et al. 2004, A&A, 418, 675
Perrin, G., Ridgway, S. T., Mennesson, B., et al. 2004, A&A, 426, 279
Perryman, M. A. C., & ESA 1997, The Hipparcos and Tycho catalogues, Publisher: Noordwijk, Netherlands: ESA Publications Division, 1997, Series: ESA SP Series vol no: 1200, ISBN: 9290923997
Petrov, R. G., Malbet, F., Weigelt, G., et al. 2003, Proc. SPIE, 4838, 924
Plez, B., Brett, J. M., & Nordlund, A. 1992, A&A, 256, 551
Plez, B., Smith, V. V., & Lambert, D. L. 1993, ApJ, 418, 812
Quirrenbach, A., Mozurkewich, D., Armstrong, J. T., Buscher, D. F., & Hummel, C. A. 1993, ApJ, 406, 215
Quirrenbach, A., Mozurkewich, D., Buscher, D. F., Hummel, C. A., & Armstrong, J.T. 1996, A&A, 312, 160
Ridgway, S. T., Joyce, R. R., White, N. M., & Wing, R. F. 1980, ApJ, 235,126
Savage, B. D., Massa, D., Meade, M., & Wesselius, P. R. 1985, ApJS, 59, 397
Tripicchio, A., Severino, G., Covino, E., Terranegra, L., & Garcia Lopez, R. J. 1997, A&A, 327, 681
Tripicchio, A., Gomez, M. T., Severino, G., et al. 1999, A&A, 345, 915
Valenti, J. A., Piskunov, N., & Johns-Krull, C. M. 1998, ApJ, 498, 851
van Belle, G., Thompson, R. R., & Creech-Eakman, M. J. 2003,
Wittkowski, M., Hummel, C. A., Johnston, K. J., et al. 2001, A&A, 377, 981 (Paper I)
Wittkowski, M., Aufdenberg, J. P., & Kervella, P. 2004, A&A, 413, 711 (Paper II)
Wittkowski, M., Hummel, C. A., Aufdenberg, J. P., & Roccatagliata, V. 2006, A&A, in press (Paper III)
Woodruff, H. C., Eberhardt, M., Driebe, T., et al. 2004, A&A, 421, 703

List of Objects